Springer

Journal of
Mechanical
Science and
Technology

Journal of Mechanical Science and Technology 23 (2009) 504~511

www.springerlink.com/content/1738-494x
DOI 10.1007/s12206-008-1102-5

# Three-dimensional model for electromigration induced evolution of flip chip solder joints †

Dongchoul Kim*

*Department of Mechanical Engineering, Sogang University, Seoul, 121-742, Korea*

(Manuscript Received July 11, 2008; Revised October 21, 2008; Accepted November 6, 2008)

**Abstract**

Recent experiments have shown failure in flip chip micro solder joints induced by electromigration. This paper proposes a computational model to simulate the evolution of micro and sub-micro scale solder joints due to electromigration induced diffusion. Complicated morphological changes of the solder bump and multiple mechanisms cause a computational challenge. This is addressed by employing a diffuse interface model with multiple concentrations. To efficiently resolve complications, a semi-implicit Fourier spectral scheme and a biconjugate-gradient method are adopted. Results have demonstrated rich dynamics and solder breakage at the interface on the cathode side.

*Keywords*: Solder joint; Electromigration; Interface energy; Diffuse interface model

## 1. Introduction

Flip chip is one of the rapidly growing microelectronics packaging technologies due to its high input/output counts, better electrical performance, high throughput and low profile. In flip chip, solder joints are the interconnection between a die and the package carrier. Along with the trend of miniaturization, the diameter of a solder joint has been reduced from 100 μm to 50 μm and smaller. The average current density easily reaches $10^4$ A/cm$^2$ and higher [1]. Under such high current density, electromigration in solder joints becomes a major concern for flip chip reliability. The transport of momentum from electrons to atoms causes a flux of metal atoms diffusing in the direction of the electron flow. At the sites of flux divergence, atoms will either deplete or accumulate, leading to the development of voids or hillocks which may cause failure of solder joints.

Experimental techniques have been developed to quantitatively investigate the electromigration process in a solder. Characteristics such as activation energy, critical length, threshold current density, effective charge numbers and electromigration rate have been measured [2, 3]. From experiments during the operation of a real flip chip, it has been also observed that void formation starts near the current crowding region of the solder contact, and spreads quickly across the contact area after nucleation [4]. Voids developed at the contact area reduce the contact cross-section. The associated increase of local current density further promotes electromigration and eventually leads to failure such as breakage. Prediction of the solder reliability demands advanced computational tools. Several studies have addressed the two-dimensional shape evolution of solder joints, where a void was assumed to have a pancake shape [5, 6].

We present a three-dimensional model for the electromigration-induced evolution of flip chip solder joints. Previous two-dimensional modeling studies assumed preexisting voids which evolve following the guided evolving directions and shapes within

† This paper was recommended for publication in revised form by Associate Editor Dae-Eun Kim

* Corresponding author. Tel.: +82 2 705 8643, Fax.: +82 2 712 0799
E-mail address: dckim@sogang.ac.kr

steady solders. Our three-dimensional dynamic model allows us to investigate the dynamic deformation of a contact region between an evolving solder bump and a flip chip. The failure time predicted with a two-dimensional model was calculated by the progress of a bar-shaped void at the contact region. It can have cases with definite deviations from the failure time calculated by the three-dimensional deformation of the contact region. Considerable change of geometry in solder during evolution and multiple mechanisms in the system cause a computational challenge. This is addressed by employing a diffuse interface model with multiple concentrations. Three concentrations generate three different regions, flip chip, solder, and air. Each region with different material properties evolves simultaneously. To efficiently resolve these complications, a robust numerical scheme is adopted.

## 2. Model

We model the electromigration-induced evolution of a solder joint and consider a lead-free solder that has been currently replacing the conventional eutectic solders. It has been considered that the elevated operating temperature may affect the evolution process of the eutectic solder joint. Generally, the effect of a high operating temperature on the eutectic solder has been investigated by increased atomic diffusivity that would accelerate the evolution process [5], or by the additional strain due to thermal expansion [7]. However, the melting point of the lead-free solder that is considered in this paper is around 218 ℃. This melting point is much higher than that of a typical eutectic solder, which is around 180 ℃. Moreover, an improved thermal management that led to the solder joint without much heat generation even with very high current density, which was around $10^4$ A/cm$^2$, was developed in experiments [7]. Furthermore, there is an experimental study which indicates that the electric current has a greater influence on even the eutectic solder joint than temperature [8]. Hence, we have not incorporated the temperature effect into the model explicitly but implicitly by the mobility of the solder. The increased mobility due to the elevated temperature will affect the calculated evolution time, which is normalized by the mobility of the solder, and the corresponding failure time.

Fig. 1 shows a schematic drawing of the flip chip solder joint sandwiched between two copper plates.

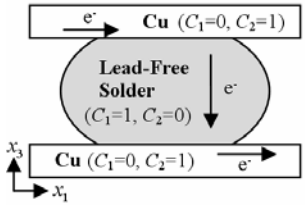


Fig. 1. A schematic drawing of a flip-chip solder joint. The two concentration fields, $C_1$ and $C_2$, represent a lead-free solder and plates, respectively.

The solder may change its morphology by diffusion via electron wind. The arrows marked by $e$ indicate the direction of electron flow. In order to efficiently present the morphological change of this system that incorporates multiple kinetics and energetics, a diffuse interface model is employed. We have demonstrated its efficiency in simulating dynamic evolutions of various nano/microstructures involving multiple mechanisms [9-12]. Here, three concentration fields, $C_1$, $C_2$, and $C_3$, are introduced to represent the lead-free solder, the copper plates, and air, respectively. We define a concentration $C_1$ by the volume fraction of the lead-free solder and a concentration $C_2$ by the volume fraction of the copper plates. Air in the domain is represented by $C_3$ which is $1-C_1-C_2$. The concentrations are regarded as spatially continuous and time-dependent functions, $C_1(x_1,x_2,x_3,t)$ and $C_2(x_1,x_2,x_3,t)$. For simplicity, we assume isotropic surface energy and diffusivity.

Following Cahn-Hilliard, the free energy of the system with multiple concentrations can be defined as

$$G=\int\left\{g_c(C_1,C_2)+h_{11}(\nabla C_1)^2 +h_{22}(\nabla C_2)^2+h_{12}(\nabla C_1\nabla C_2)\right\}dV\ . \quad (1)$$

The first term represents the chemical energy in the system. Other terms account for the interfacial energy between three components, where $h_{11}$, $h_{22}$, and $h_{12}$ are material constants. Atoms diffuse in the solder bump from high chemical potential regions to low chemical potential regions, which causes the solder bump to change its shape. The corresponding driving forces for diffusion in the solder bump and the plates are attributed to the chemical potential by $\mathbf{F}_1^{chem}=-\nabla\mu_1^0$ and $\mathbf{F}_2^{chem}=-\nabla\mu_2^0$, respectively. The chemical potential is related to the free energy by $\mu_1^0=\delta G/\delta C_1$ and $\mu_2^0=\delta G/\delta C_2$. In an electric

field, one driving force is attributed to the electron wind force. Thus, the total driving force can be expressed by $\mathbf{F}_1 = \mathbf{F}_1^{chem} + \mathbf{F}_1^{elec}$ and $\mathbf{F}_2 = \mathbf{F}_2^{chem} + \mathbf{F}_2^{elec}$, where $\mathbf{F}_1^{elec}$ and $\mathbf{F}_2^{elec}$ are the driving force related with the electric field in the solder bump and the plates, respectively. The total driving force leads to the atomic flux of $\mathbf{J}_1 = M_1\mathbf{F}_1$ and $\mathbf{J}_2 = M_2\mathbf{F}_2$. By combining with the mass conservation relation, $\partial C_1/\partial t + \nabla\cdot\mathbf{J}_1 = 0$ and $\partial C_2/\partial t + \nabla\cdot\mathbf{J}_2 = 0$, Cahn Hilliard equations are obtained as follows:

$$\frac{\partial C_1}{\partial t} = \nabla\left[ M_1\left\{ \nabla\left( \frac{\delta g_c}{\delta C_1} - 2h_{11}\nabla^2 C_1 - h_{12}\nabla^2 C_2 \right) + \mathbf{F}_1^{elec} \right\} \right], \quad (2)$$

$$\frac{\partial C_2}{\partial t} = \nabla\left[ M_2\left\{ \nabla\left( \frac{\delta g_c}{\delta C_2} - 2h_{22}\nabla^2 C_2 - h_{12}\nabla^2 C_1 \right) + \mathbf{F}_2^{elec} \right\} \right], \quad (3)$$

The electron-wind force refers to the effect of the momentum exchange between the moving electrons and the ionic atoms and is described as

$$\mathbf{F}_1^{elec} = -f_1^e\nabla\phi\,, \quad \mathbf{F}_2^{elec} = -f_2^e\nabla\phi\,, \quad (4)$$

where $f_1^e = |e|Z_1^*/\Omega_1$ and $f_2^e = |e|Z_2^*/\Omega_2$. $\Omega_1$ and $\Omega_2$ are the atomic volume of tin and copper, respectively. $Z_1^*$ and $Z_2^*$ are the phenomenological effective valence of the atom of tin and copper, respectively. $e$ is the charge of an electron. The negative signs in equations mean that the force is in the direction of the electron flow. Due to the conservation of electric charges and Ohm's law, the electric potential obeys the Laplace equation,

$$\nabla\cdot\left\{ \xi\left(C_1, C_2\right)\nabla\phi \right\} = 0\,, \quad (5)$$

where $\xi$ is the conductivity of the media, which is linearly interpolated by that of the solder bump and the copper plates, namely, $\xi(C) = \xi_1 C_1 + \xi_2 C_2$. This partial differential equation, together with boundary conditions, determines the electric potential.

The chemical energy with three components has been derived from the studies of two-phase solidification [13]:

$$+a_1\frac{C_1^2}{4}\left\{ 15(1-C_1)\left(1+C_1-(C_3-C_2)^2\right) + C_1\left(9C_1^2-5\right) \right\}$$
$$+a_2\frac{C_2^2}{4}\left\{ 15(1-C_2)\left(1+C_2-(C_3-C_1)^2\right) + C_2\left(9C_2^2-5\right) \right\}$$
$$+a_3\frac{C_3^2}{4}\left\{ 15(1-C_3)\left(1+C_3-(C_1-C_2)^2\right) + C_3\left(9C_3^2-5\right) \right\}. \quad (6)$$

By taking $a_1 = a_2 = a_3 = 1$ for simplicity and $C_3 = 1 - C_1 - C_2$, the chemical potentials are expressed by

$$\frac{\partial g_c}{\partial C_1} = f_0\left\{ 2(2C_1 + C_2 - 1)\left(2C_1^2 - 2C_1 + 2C_1C_2 - C_2 + 2C_2^2\right) \right\}, \quad (7)$$

$$\frac{\partial g_c}{\partial C_2} = f_0\left\{ 2(C_1 + 2C_2 - 1)\left(2C_1^2 - C_1 + 2C_1C_2 - 2C_2 + 2C_2^2\right) \right\}. \quad (8)$$

By normalization with the characteristic length, $L_c$, time, $t_c$,

$$\frac{\partial C_1}{\partial t} = \nabla\left\{ M_1\nabla\left( \mu_1^0 - Ch_{11}^2\nabla^2 C_1 - \frac{1}{2}Ch_{12}^2\nabla^2 C_2 - E\phi \right) \right\}, \quad (9)$$

$$R_M\frac{\partial C_2}{\partial t} = \nabla\left\{ M_2\nabla\left( \mu_2^0 - Ch_{22}^2\nabla^2 C_2 - \frac{1}{2}Ch_{12}^2\nabla^2 C_1 - E\phi \right) \right\}, \quad (10)$$

where the chemical potentials are $\mu_1^0 = (2C_1 + C_2 - 1)\left(2C_1^2 - 2C_1 + 2C_1C_2 - C_2 + 2C_2^2\right)$ and $\mu_2^0 = (C_1 + 2C_2 - 1)\left(2C_1^2 - C_1 + 2C_1C_2 - 2C_2 + 2C_2^2\right)$. The characteristic variables are $t_c = L_c^2/2M_{1c}f_0$, $Ch_{11} = h_{11}/L_c^2 f_0$, $Ch_{12} = h_{12}/L_c^2 f_0$, and $Ch_{22} = h_{22}/L_c^2 f_0$. $R_M$ is the ratio of the characteristic mobilities, $R_M = M_{1c}/M_{2c}$ and $E = \phi_c/2f_0$. $Ch_{11}$, $Ch_{22}$, and $Ch_{12}$ are the Cahn numbers which represent the relative significance of the interface energy between materials.

## 3. Numerical implementation

The numerical approach needs to have a high spatial resolution to resolve the high order derivatives in the diffusion equation as well as the large gradients at the interface region. The approach should also be efficient and stable for the time integration, which is especially important for three-dimensional simulations. We propose an efficient semi-implicit Fourier spectral method for both high spatial resolution and fast computation. The central idea of the semi-implicit method is to treat the linear term implicitly and the nonlinear term explicitly to allow for larger time steps without losing numerical stability [14, 15]. In contrast, a fully implicit treatment yields expensive

schemes while explicit discretization quickly leads to numerical instability or needs impractical time-step constraint,

$$\frac{\partial C_1}{\partial t} = 2\tau_1\nabla^2 C_1 + \tau_1\nabla^2 C_2 - Ch_{11}^2\nabla^4 C_1 - \frac{1}{2}Ch_{12}^2\nabla^4 C_2 + \left\{\nabla\cdot M_1\nabla\left(\mu_1^0 - Ch_{11}^2\nabla^2 C_1 - \frac{1}{2}Ch_{12}^2\nabla^2 C_2 - E\phi\right) - 2\tau_1\nabla^2 C_1 - \tau_1\nabla^2 C_2 + Ch_{11}^2\nabla^4 C_1 + \frac{1}{2}Ch_{12}^2\nabla^4 C_2\right\}, \quad (11)$$

$$R_M\frac{\partial C_2}{\partial t} = 2\tau_2\nabla^2 C_2 + \tau_2\nabla^2 C_1 - Ch_{22}^2\nabla^4 C_2 - \frac{1}{2}Ch_{12}^2\nabla^4 C_1 + \left\{\nabla\cdot M_2\nabla\left(\mu_2^0 - Ch_{22}^2\nabla^2 C_2 - \frac{1}{2}Ch_{12}^2\nabla^2 C_1 - E\phi\right) - 2\tau_2\nabla^2 C_2 - \tau_2\nabla^2 C_1 + Ch_{22}^2\nabla^4 C_2 + \frac{1}{2}Ch_{12}^2\nabla^4 C_1\right\} \quad (12)$$

Note that stability is achieved in conjunction with the extrapolated Gear (SBDF) scheme for time integration. Among the second order multi-step methods, SBDF has the strongest high modal decay [16]. This provides the required damping for the very high frequencies in the diffusion equation without a harsh time-step constraint. Applying the scheme to the normalized diffusion equation, we obtain the following discretized form:

$$\frac{3}{2}C_1^{n+1} - 2C_1^n + \frac{1}{2}C_1^{n-1} = \Delta t\left(2\tau_1\nabla^2 C_1^{n+1} + \tau_1\nabla^2 C_2^{n+1} - Ch_{11}^2\nabla^4 C_1^{n+1} - \frac{1}{2}Ch_{12}^2\nabla^4 C_2^{n+1}\right) + 2P_1^n - P_1^{n-1}, \quad (13)$$

$$\frac{3}{2}C_2^{n+1} - 2C_2^n + \frac{1}{2}C_2^{n-1} = \frac{\Delta t}{R_M}\left(2\tau_2\nabla^2 C_2^{n+1} + \tau_2\nabla^2 C_1^{n+1} - Ch_{22}^2\nabla^4 C_2^{n+1} - \frac{1}{2}Ch_{12}^2\nabla^4 C_1^{n+1}\right) + 2P_2^n - P_2^{n-1}. \quad (14)$$

where

$$P_1^n = \Delta t\left\{\nabla\cdot M_1\nabla\left(\mu_1^{0n} - Ch_{11}^2\nabla^2 C_1^n - Ch_{12}^2\nabla^2 C_2^n/2 - E\phi\right) - 2\tau_1\nabla^2 C_1^n - \tau_1\nabla^2 C_2^n + Ch_{11}^2\nabla^4 C_1^n + Ch_{12}^2\nabla^2 C_2^n/2\right\}, \quad (15)$$

$$P_2^n = \left(\Delta t/R_M\right)\left\{\nabla\cdot M_2\nabla\left(\mu_2^{0n} - Ch_{22}^2\nabla^2 C_2^n - Ch_{12}^2\nabla^2 C_1^n/2 - E\phi\right) - 2\tau_2\nabla^2 C_2^n - \tau_2\nabla^2 C_1^n + Ch_{22}^2\nabla^4 C_2^n + Ch_{12}^2\nabla^2 C_1^n/2\right\}. \quad (16)$$

By applying the Fourier transform to Eqs. (13) and (14), we effectively perform calculations with

$$\hat{C}_1^{n+1} = \frac{1}{Det}\left\{L_4\left(2\hat{C}_1^n - \frac{1}{2}\hat{C}_1^{n-1} + 2\hat{P}_1^n - \hat{P}_1^{n-1}\right) - L_2\left(2\hat{C}_2^n - \frac{1}{2}\hat{C}_2^{n-1} + 2\hat{P}_2^n - \hat{P}_2^{n-1}\right)\right\}, \quad (17)$$

$$\hat{C}_2^{n+1} = \frac{1}{Det}\left\{-L_3\left(2\hat{C}_1^n - \frac{1}{2}\hat{C}_1^{n-1} + 2\hat{P}_1^n - \hat{P}_1^{n-1}\right) + L_1\left(2\hat{C}_2^n - \frac{1}{2}\hat{C}_2^{n-1} + 2\hat{P}_2^n - \hat{P}_2^{n-1}\right)\right\}, \quad (18)$$

where $L_1 = 3/2 + 2\tau_1\Delta tk^2 + Ch_{11}^2\Delta tk^4$, $L_2 = \tau_1\Delta tk^2 + Ch_{12}^2\Delta tk^4/2$, $L_3 = \tau_2\Delta tk^2/R_M + Ch_{12}^2\Delta tk^4/(2R_M)$, $L_4 = 3/2 + 2\tau_2\Delta tk^2/R_M + Ch_{22}^2\Delta tk^4/R_M$, $Det = L_1L_4 - L_2L_3$. The caret '^' stands for the Fourier Transform, and $k^2 = k_1^2 + k_2^2 + k_3^2$. The electric field is determined by $\nabla\cdot\left\{\xi\left(C_1, C_2\right)\nabla\phi\right\} = 0$, which can also be written as $\xi\nabla^2\phi + \nabla\xi\cdot\nabla\phi = 0$. We apply the second order discretization and compute the matrix with the preconditioned biconjugate gradient method [17]. The Jacobi preconditioner is adopted. The approach allows efficient computation of large 3D domains.

In the following, we outline the procedure to compute $C_1^{n+1}$ and $C_2^{n+1}$ from $C_1^n$ and $C_2^n$. First, we compute the electric potential field $\phi^n$ that corresponds to the concentration distributions $C_1^n$ and $C_2^n$. Then, using the solution of $\phi^n$, we compute $\left(\mu_1^c\right)^n$ and $\left(\mu_2^c\right)^n$. Using $\hat{C}_1^n$, $\hat{C}_2^n$, and $\hat{\phi}^n$, we compute the convective Cahn-Hilliard equation in Fourier space to obtain $\hat{C}_1^{n+1}$ and $\hat{C}_2^{n+1}$. The new concentrations $C_1^{n+1}$ and $C_2^{n+1}$ are obtained from $\hat{C}_1^{n+1}$ and $\hat{C}_2^{n+1}$ by the inverse Fourier transform. The procedure is repeated until a prescribed time.

## 4. Results and discussions

The proposed three-dimensional model and numerical approach allow a comprehensive computational study of the dynamic evolution of solder joints. Representative results are presented in this section. The calculation domain size is 70×70×50. The diameter of the solder bump is 50, which corresponds to a physical diameter of 50 μm since the characteristic length is taken to be 1 μm. The plates at the top and the bottom of the solder have a thickness of 5. Visual-

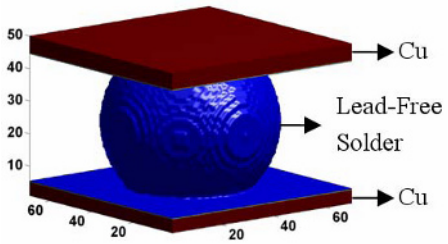


Fig. 2. The three-dimensional graphs are visualized by tracking where $C_1$ and $C_2$ have 0.5. In the solder region, $C_1$ becomes one and $C_2$ becomes zero while $C_1$ becomes zero and $C_2$ becomes one in the plates region.

ized three-dimensional graphs represent the solder surface and the plates by tracking where $C_1$ and $C_2$ have 0.5 as shown in Fig. 2.

Fig. 3 shows an evolution sequence from $t = 0$ to $t = 10000$ when the electric field is not applied with different combination of the surface energies. Since the diffusivity of Cu at 150 °C is around $10^{-12}$ cm$^2$/s and that of Sn is $1.3\times10^{-10}$ cm$^2$/s, the plates diffuse slowly and almost remain flat while the solder bump undergoes the morphological evolution during simulation. Fig. 3(a) shows an evolution when the interface energies between the solder bump, the plates, and air are equal; $Ch_{11} = 1.0$, $Ch_{22} = 1.0$, and $Ch_{12} = 1.0$. If a separated solder bump is considered, the solder bump should evolve into a spherical shape to minimize its surface energy. However, there is the interface energy at the contact area between the solder bump and the plates, which plays an important role during the evolution process. As shown in Fig. 3(a), when the interface energies of solder, the plates, and the contact area are equal, the whole system can be regarded as a single structure. Thus, the solder bump evolves into a cylindrical shape and the contact area increases to minimize the total interface energy of the system. As the interface energy of the contact area becomes smaller than that of the solder and the plate as shown in Fig. 3(b) and (c), the contact area does not increase and the solder bump tends to remain a spherical shape to reduce its surface energy, which is larger than that of the contact area. The reliability of solder joints correlates with the contact area, which is considerably dependent on the relation between the interface energies of each materials. Hence, chemical or geometric manipulations to increase the interface energy between the solder and the plates will improve the reliability of the solder joint. As shown in Fig.

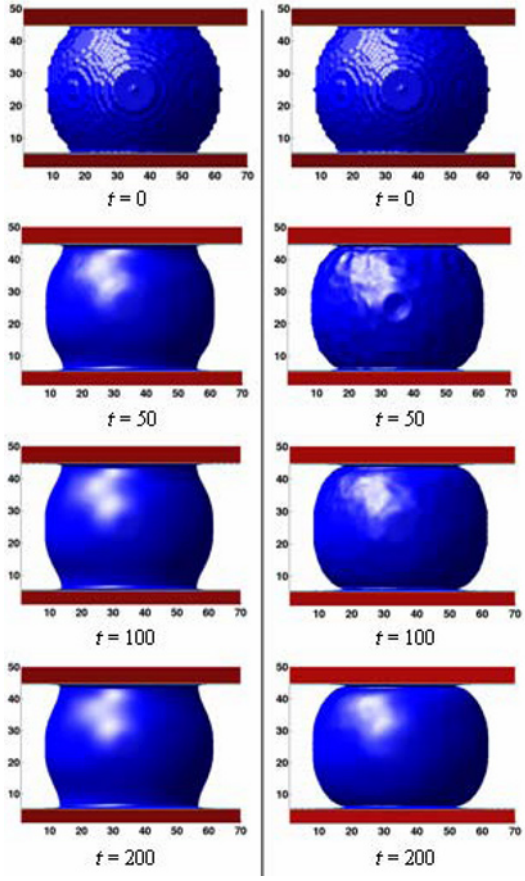


(a) (b)

Fig. 3. The simulation results with different combinations of Cahn numbers; (a) $Ch_{11} = 1.0$, $Ch_{22} = 1.0$, $Ch_{12} = 1.0$, and (b) $Ch_{11} = 1.0$, $Ch_{22} = 1.0$, $Ch_{12} = 0.1$.

3(c), when the Cahn numbers are assigned as $Ch_{11} = 1.0$, $Ch_{22} = 1.0$, and $Ch_{12} = 0.1$, which the surface energy between the solder bump and the plates is 10 times smaller than those of the solder bump and the plates, the simulation without an electric field shows a reasonably maintained spherical shape of the solder bump for a long time, similar to empirical observations. Thus, the Cahn numbers of $Ch_{11} = 1.0$, $Ch_{22} = 1.0$, and $Ch_{12} = 0.1$ are assigned in the following simulations.

Fig. 4 presents the evolution of solder joints under an electric field. Electron wind flows from the left of the top plate to the right of the bottom plate as shown in Fig. 1. The solder bump is subjected to a normalized electric potential of 1 that corresponds to the current density of $10^4$ A/cm$^2$, which is typical in experiments. The current crowding occurs at the contact

region between the top plate and the solder bump. As shown by experimental study, the formation of a void is observed at this contact area. In our simulations, the solder bump starts to break apart from the top plate at the left side of the solder bump. This simulation result is consistent with experimental observations in which a void tends to initiate where current crowding occurs. When a void forms, it blocks the original electrical path and changes the current-crowding region to travel around the void. The growth of the void reduces the effective contact area at the interface region and increases the current density in the remaining contact area. Then, this void will make the current density higher and eventually cause circuit failure. In simulations, the contact area between the solder bump and the top plate decreases. The evolution sequence shows that the electron wind causes solder material to diffuse from top to bottom, from cathode to anode.

In Fig. 5, we calculate the failure time by the contact area between the solder bump and the top plate applying various strengths of the electric field. Fig. 5(a) shows the decreasing contact area as time goes on and the stronger electric field induces the quickly decreasing contact area, which leads to the accelerated failure time. As shown in Fig. 5(b), the failure time is almost exponentially decreased as the strength of the applied electric field increases. The characteristic time is normalized by the mobility of the solder. The increased operating temperature will induce the high mobility, which will decrease the characteristic time and eventually the corresponding failure time. Hence, the cases with the same solder joint under different operating temperatures will have different failure times.

To investigate the effect of the designed top plates, we have performed simulations with patterned plates. Fig. 6 shows the designed surfaces and the corresponding initial solders. The top plate is designed with stripes or bumps. Patterns have a width of 5 and a depth of 8. Stripes are patterned in the $x_1$ and $x_2$ directions to investigate the effect of the patterned direction. The electrons flow from the left of the top plate to the right of the bottom plate along the $x_1$ direction as shown in Fig. 1. Thus, the stripe pattern in Fig. 6(a) has the direction normal to the direction

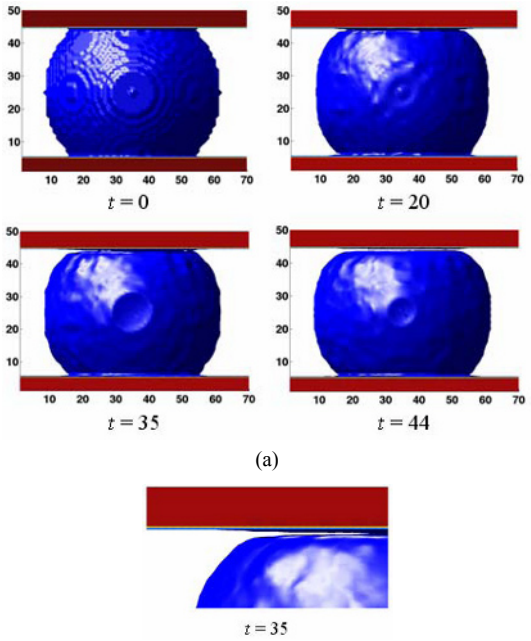


Fig. 4. (a) The simulated evolution of the solder joint is presented. (b) The solder bump starts to break apart from the top plate at the left side of the solder bump. The assigned Cahn numbers are $Ch_{11}$ = 1.0, $Ch_{22}$ = 1.0, and $Ch_{12}$ = 0.1.

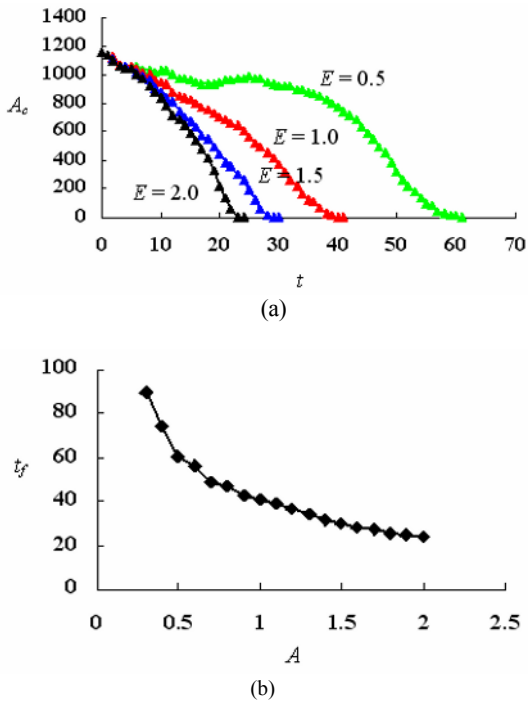


Fig. 5. (a) The contact region between the solder bump and the top plate ($A_c$) is plotted as a function of time with different strengths of the applied electric fields ($E$). (b) The failure time ($t_f$) is exponentially decreased as the strength of the applied electric field increases. The assigned Cahn numbers are $Ch_{11}$ = 1.0, $Ch_{22}$ = 1.0, and $Ch_{12}$ = 0.1.

Table 1. The failure times are calculated from the simulations with different designed patterns on the top plate.

| Geometry | Area (initial) | Time (failure) |
|---|---|---|
| Flat | 1153 | 36 |
| Stripes ( $x_1$ ) | 4728 | 230 |
| Stripes ( $x_2$ ) | 4728 | 216 |

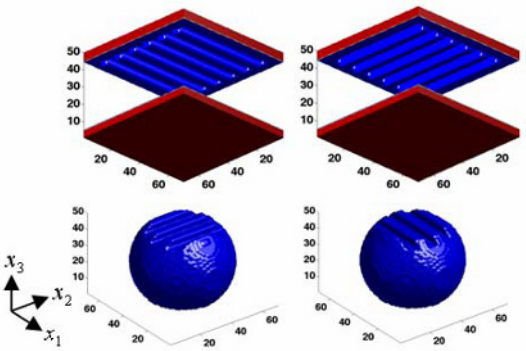


(a) (b)

Fig. 6. The designed surfaces of the top plates. (a) The top plate is patterned with stripes having a width of 5 and a depth of 8 in the $x_1$ direction and (b) in the $x_2$ direction.

of the electron flow. Our three-dimensional model makes it possible to study the effect of various patterns. The contact area with the flat top surface as shown in Fig. 4 is 1153, and the area of the contact region is increased by the designed patterns in Fig. 6(a) and (b), which becomes 4728. As shown in Table 1, the solder joint with the designed patterns shows improved reliability than that without a pattern. The contact area without a pattern decreases and becomes a considerably smaller contact area, which is 100 at $t = 36$, while that with the designed pattern becomes the same size of contact area at over $t = 200$. The solder joint with the designed patterns takes approximately 6 times more time than that without a pattern to reduce its contact area to a very small area, which can cause the failure. The designed patterns on the top plate increase the contact area between the solder bump and the top plate where the failure happens. The increased contact area increases the interface energy of the contact area, which leads to increased reliability of the solder joints.

The simulation results also present the effect of the pattern geometry. Comparing the results with the stripe pattern having a width of 5, the solder with the strip pattern in the $x_1$ direction that is normal to the direction of the electron flow shows better reliability than that with the strip pattern in the $x_2$ direction even though they have the same contact area.

The stripe pattern in the $x_1$ direction lengthens the path of the electron flow at the contact area so that it takes more time for mass transport driven by the electron flow. This simulation result suggests that the evolution of the solder joint cannot be determined only by energetics but also it is limited by the kinetic process. These simulations suggest that the reliability of solder joints can be significantly improved by the well-designed plates.

## 5. Conclusions

We have presented a three-dimensional model for the evolution of flip chip solder joints induced by electromigration. The developed three-dimensional dynamic model allows us to investigate the dynamic deformation of the contact region between the evolving solder bump and the plate. The solder bump starts to break apart from the current crowding region. The different evolving processes of the solder bump are presented as different strengths of the electric field are applied. The failure time is decreased as the strength of the applied electric field increases. Moreover, using the developed three-dimensional model, we can investigate the effect of the designed geometry of the top plate on the reliability of solder joints. From three-dimensional simulations, it is presented that the reliability of the solder joint is significantly influenced by the increased contact area by the designed pattern of the top plate and the kinetic path that is developed in a specific direction by the designed pattern. This study provides an effective model which presents dynamic evolution process of solder joints and can be a solid base for further analysis incorporating additional mechanisms.

## Acknowledgment

This work was supported by the Sogang University Research Grant of 2007118.

## References

[1] K. N. Tu, Recent advances on electromigration in very-large-scale-integration of interconnects, *J. Appl. Phys.* 94 (9) (2003) 5451-5473.

[2] Y. T. Yeh, C. K. Chou, et al., Threshold current

density of electromigration in eutectic SnPb solder, *Appl. Phys. Lett.* 86 (20) (2005) 203504..

[3] C. Basaran, H. Ye, et al., Failure modes of flip chip solder joints under high electric current density, *J. Elect. Pack.* 127 (2) (2005) 157-163.

[4] E. C. C. Yeh, W. J. Choi, et al., Current-crowding-induced electromigration failure in flip chip solder joints, *Appl. Phys. Lett.* 80 (4) (2002) 580-582..

[5] L. Zhang, S. Ou, et al., Effect of current crowding on void propagation at the interface between intermetallic compound and solder in flip chip solder joints, *Appl. Phys. Lett.* 88 (1) (2006) 012106..

[6] S. W. Liang, Y. W. Chang, et al., Effect of three-dimensional current and temperature distributions on void formation and propagation in flip-chip solder joints during electromigration, *Appl. Phys. Lett.* 89 (2) (2006) 022117.

[7] H. Ye, C. Basaran, et al., Deformation of solder joint under current stressing and numerical simulation, *Int. J. Sol. Struct.* 41 (18-19) (2004) 4939-4958.

[8] H. Ye, C. Basaran, et al., Pb phase coarsening in eutectic Pb/Sn flip chip solder joints under electric current stressing, *Int. J. Sol. Struct.* 41 (2004) 2743-2755.

[9] D. Kim and W. Lu, Three-dimensional model of electrostatically induced pattern formation in thin polymer films, *Phys. Rev. B* 73 (3) (2006) 035206.

[10] D. Kim and W. Lu, Creep flow, diffusion, and electromigration in small scale interconnects, *J. Mech. Phys. Solids* 54 (12) (2006) 2554-2568.

[11] W. Lu and D. Kim, Engineering nanophase self-assembly with elastic field, *Acta. Mater* 53 (13) (2005) 3689-3694.

[12] W. Lu and D. Kim, Patterning nanoscale structures by surface chemistry, *Nano Lett.* 4 (2) (2004) 313-316.

[13] R. Folch and M. Plapp, Quantitative phase-field modeling of two-phase growth, *Phys. Rev. E* 72 (2) (2005) 011602.

[14] W. Lu and Z. Suo, Dynamics of nanoscale pattern formation of an epitaxial monolayer, *J. Mech. Phys. Solids* 49 (9) (2001) 1937-1950.

[15] J. Zhu, L.-Q. Chen, et al., Coarsening kinetics from a variable-mobility Cahn-Hilliard equation: Application of a semi-implicit Fourier spectral method, *Phys. Rev. E* 60 (4) (1999) 3564-3572.

[16] U. M. Ascher, S. J. Ruuth, et al., Implicit-explicit methods for time dependent partial differential equations, *SIAM J. Numer. Annal.* 32 (3) (1995) 797-823.

[17] G. H. Golub and C. F. V. Loan, *Matrix computation*, Johns Hopkins University Press, Baltimore, (1989).

**Dongchoul Kim** received a B.S. degree in Mechanical Engineering from Yonsei University in 2000. He then went on to receive his M.S. and Ph.D. degrees from The University of Michigan in 2003 and 2005, respectively. Dr. Kim is currently an Assistant Professor at the School of Mechanical Engineering at Sogang University in Seoul, Korea. Dr. Kim's research interests are in the area of computational analysis of micro/nanostructures.